

Motion Gradient Vector Flow: An External Force for Tracking Rolling Leukocytes With Shape and Size Constrained Active Contours

Nilanjan Ray*, *Member, IEEE* and Scott T. Acton, *Senior Member, IEEE*

Abstract—Recording rolling leukocyte velocities from intravital microscopic video imagery is a critical task in inflammation research and drug validation. Since manual tracking is excessively time consuming, an automated method is desired. This paper illustrates an active contour based automated tracking method, where we propose a novel external force to guide the active contour that takes the hemodynamic flow direction into account. The construction of the proposed force field, referred to as motion gradient vector flow (MGVF), is accomplished by minimizing an energy functional involving the motion direction, and the image gradient magnitude. The tracking experiments demonstrate that MGVF can be used to track both slow- and fast-rolling leukocytes, thus extending the capture range of previously designed cell tracking techniques.

Index Terms—Active contour, anisotropic diffusion, gradient vector flow, intravital m, leukocyte rolling velocity.

I. INTRODUCTION

BIO MEDICAL research groups studying inflammation need reliable automated methods for tracking rolling leukocytes from intravital (observed in living animal) microscopic video, because rolling velocity is a principal indication of the inflammatory response [22], and manual methods of tracking require tens of hours of user interactive image processing per intravital experiment. Fig. 1 shows six successive video frames of the microscopic observations in a postcapillary venule of the cremaster muscle [18] of a mouse. The figure shows the microvessel and the round shaped leukocytes rolling in the bloodstream. The hurdles in the way of automated tracking of these rolling leukocytes can be enumerated: 1) Leukocytes roll within a moving “background” (platelets, plasma, erythrocytes, inactivated leukocytes, etc.). These additional components lead to severe clutter. 2) Leukocytes slowly deform in shape as they roll along a venule, so the objects to be tracked here are not rigid, but deformable. 3) Breathing movements of the living subject introduce jitter in the video making the automated tracking process more difficult and

requiring video registration. 4) Changes in transillumination, cells moving in and out of the focal plane, and breathing movements of the living subject lead to contrast changes (bright cells versus dark cells).

Whereas cell tracking *in vitro* (in a flow chamber, for example) is feasible with centroid based [9], [12] and correlation based [4], [10], [15], [17], [26], and more recently with active contour based methods [32], the experiments show that centroid and correlation based methods are not well equipped for the *in vivo* equipped for the *in vivo* (observed within living animal) leukocyte tracking problem [14]. Being a relatively nascent field of research, there exist only a few attempts at automated tracking of leukocytes from intravital video microscopy – centroid and correlation based adaptive template matching techniques [1], [3], [14], leukocyte trace detection by spatiotemporal image formation [25], shape and size constrained active contour based method [22]. It has been demonstrated that the shape and size constrained active contours governed by gradient vector flow (GVF) [31] type external forces are superior in automated rolling leukocyte tracking to the aforementioned methods in terms of localization and the fraction of frames tracked successfully [14].

However, we find that the effectiveness of GVF force in conjunction with shape and size constrained active contour decreases with decreasing temporal resolution of the intravital videos. And the tracker described in [22] has a greater tendency to lose fast rolling cells that have interframe displacements greater than one cell radius. When interframe leukocyte displacement is large, [22] proposes to utilize a Dirichlet boundary condition in order to compute GVF type external force for active contour evolution. This boundary condition essentially biases the direction of vector diffusion away from the initial contour [23]. We note that in order to apply this method one needs to know *a priori* whether the interframe leukocyte displacement exceeds a leukocyte radius, because when the leukocyte displacement is less than a cell radius, GVF computation with the Dirichlet boundary condition does not yield the desired result [20]. Alternatively, depending on some criterion, such as average edge magnitude computed over the length of the contour, two active contours can be used in conjunction – one contour computed with the Dirichlet boundary condition and another without the Dirichlet boundary condition.

Unlike our previous tracking proposal in [22], the new external force, motion gradient vector flow (MGVF) proposed here, does not need to know in advance whether the interframe leukocyte displacement is small (interframe displacement less

Manuscript received March 3, 2004; revised July 27, 2004. This work was supported in part by the National Institutes of Health (NIH) under Grant HL68510. The Associate Editor responsible for coordinating the review of this paper and recommending its publication was E. Meijering. *Asterisk indicates corresponding author.*

*N. Ray is with the Department of Electrical and Computer Engineering, University of Virginia, 351 McCormick Road, Charlottesville, VA 22904 USA (e-mail: nray@virginia.edu).

S. T. Acton is with the Department of Electrical and Computer Engineering/Biomedical Engineering, University of Virginia, Charlottesville, VA 22904 USA (e-mail: acton@virginia.edu)

Digital Object Identifier 10.1109/TMI.2004.835603

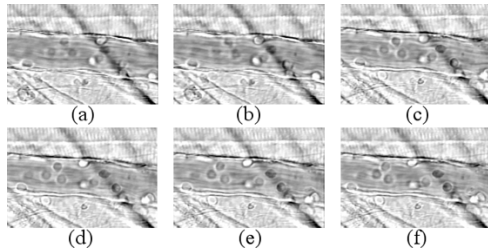


Fig. 1. (a)–(f) 1st, 4th, 7th, 10th, 13th and 16th frame of an intravital video sequence showing rolling leukocytes in a mouse venule.

than one cell radius) or large (interframe displacement between one cell radius and one cell diameter). The impact of MGVF is shown to be twofold: 1) for fixed frame rates, MGVF facilitates tracking of fast as well as slow rolling leukocytes; 2) for slow rolling leukocytes, if frame rate is decreased, MGVF can achieve the same, if not better, tracking performance of GVF at the original frame rate. MGVF and GVF tracking involve about the same computational cost per video frame; thus, at a low temporal resolution, MGVF is more attractive in terms of computational cost.

While GVF and MGVF methods are based on edge (gradient) information of the leukocytes, an alternative approach will be to utilize region based information such as the intensity profile inside and/or outside of the leukocyte. Such methods have been popular in general image segmentation [7], [29]. Chakraborty *et al.* utilize an integrated edge and region based information for image segmentation [6]. However, note from Fig. 2(a) that the image intensity inside a leukocyte varies widely. And as mentioned before, note also that a leukocyte may appear dark or bright. The blood flow and the presence of muscle striations contribute to the inhomogeneity of the intensity profile inside and outside of the leukocyte in the intravital imagery [see Fig. 2(a)]. The gradient magnitude image in Fig. 2(b) shows that leukocyte edges are prominent with round/elliptic shapes. When the leukocytes appear as dark, we observe that the intensity profile inside the leukocyte closely resembles that of the exterior. In such cases, an annular structure (often broken in appearance) separates inside and outside the leukocyte. These visual cues suggest that region based active contour methods may not be an ideal choice for the problem at hand. And we thus rely on edge based information for leukocyte tracking and put forth a new method (MGVF).

Before introducing MGVF, let us first describe the basic cell tracking framework used in [22].

Algorithm 1

- 1) *Leukocyte detection*: To initiate this algorithm, a leukocyte on the first frame is detected either manually or automatically as in [21], and then shape-size constrained contour evolution is performed to delineate the leukocyte.
- 2) *Tracking*: From the second frame onwards, for each frame execute steps 2a) and 2b):
 - a) *Initial active contour placement*: The final contour delineating the

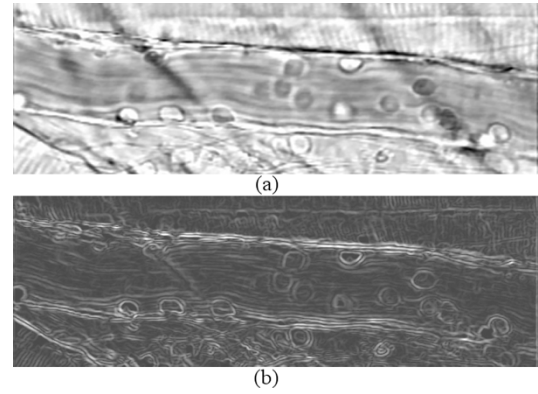


Fig. 2. (a) Leukocytes, (b) gradient magnitude of the leukocyte image. Leukocytes are seen to appear as dark or bright in the intravital microscopic videos. Gray level varies widely inside a leukocyte. Leukocyte edges are more prominent than homogeneity of intensity inside leukocytes.

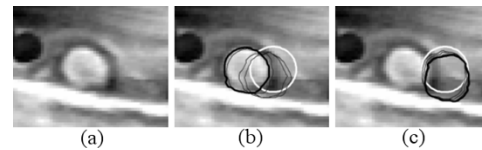


Fig. 3. (a) A rolling leukocyte, (b) success of GVF active contour, (c) failure of GVF active contour. White and black contours, respectively, represent initial and final contours, and gray contours represent the active contour evolution process.

leukocyte from the previous frame is placed over the current video frame.

- b) *Active contour evolution*: Starting from the initial active contour, a shape-size constrained contour evolution is performed on the current video frame to delineate the displaced rolling leukocyte.

For a fixed frame rate, higher rolling velocity leads to greater displacement of the contour. Fig. 3(a) shows a rolling leukocyte. Fig. 3(b) shows the evolution of a shape-size constrained active contour governed by GVF. In this case, the active contour is successful in capturing the leukocyte since the frame-to-frame displacement is small. Fig. 3(c) shows the same leukocyte with a different initial contour that is displaced farther from the leukocyte; such a situation in the aforementioned tracking algorithm (**Algorithm 1**) arises when the leukocyte rolling velocity is high. In this case we observe that the GVF active contour fails to capture the leukocyte. One potential remedy is to advance the initial contour in the blood flow direction before contour evolution. The distance, with which the contour is to be advanced, has to be estimated. Such estimation is nontrivial since it is not uncommon that a single leukocyte shows a complex trait of slow and fast movements (microbursts) as it interacts with the endothelium [16]. Moreover, jitter and excessive clutter in the intravital video also contribute to the difficulty of estimating the subsequent leukocyte position. It should also be noted that step 2b) of **Algorithm 1** implicitly assumes that the leukocytes are not occluding one another.

Instead of moving the initial active contour via a prediction mechanism such as the Kalman filter [14], in our approach, we

introduce a new active contour external force that can accommodate both the fast and the slowly rolling leukocytes simultaneously. The basic GVF mechanism uses the gradient of an image edge map and diffuses the gradients so that a boundary can be captured if the initial contour is not placed directly in the neighborhood of the desired boundary. The effect of GVF is that the vectors “point” the active contour in the direction of the closest major boundary; these vectors are used as the active contour external force. In MGVF, we follow this approach and bias the diffusion of these vectors in the direction of flow. In other words, if the diffusion of the GVF vectors is favored more in the direction of blood flow, then, even if the initial contour lags behind the leukocyte center, it will sense the gradient magnitude slope and will recover the leukocyte shape.

Before detailing MGVF in Section III, we first summarize the necessary background for the shape and size constrained active contours and the standard GVF technique.

II. BACKGROUND

A. Shape-Size Constrained Active Contour

Since rolling leukocytes appear as slightly deformed circles in the intravital video frames, a natural choice for delineating the leukocyte boundary is to utilize a shape and size constrained active contour with a suitable external force such as GVF [22]. In this paper, we adopt the same notion of shape and size constraints and express the active contour as a parametric curve via a reference point, (P, Q) , and the polar coordinates $(R(t), t)$, so that the Cartesian coordinates of the contour points become: $(P + R(t) \cos(t), Q + R(t) \sin(t))$. Such a radial active contour is depicted in Fig. 4. We want this active contour to be collocated with positions of high gradient magnitude in the image, and not to deviate significantly from a circular shape of a desired radius, which can be obtained *a priori* from the known leukocyte radius (~ 4 microns) and the spatial resolution of the video. The active contour achieves the goal of delineating a leukocyte by minimizing the following energy functional:

$$E_{r\text{-snake}}(P, Q, R) = E_{\text{edge}}(P, Q, R) + \mu_{\text{cons}} E_{\text{cons}}(R) + \mu_{\text{pos}} E_{\text{pos}}(P, Q, R) \quad (1)$$

where

$$E_{\text{edge}}(P, Q, R) = -\frac{1}{L_s} \times \int_0^{2\pi} w(P + R(t) \cos(t), Q + R(t) \sin(t)) R(t) dt \quad (2)$$

$$E_{\text{cons}}(R) = \frac{1}{2} \int_0^{2\pi} (R(t) - \rho)^2 dt \quad (3)$$

and

$$E_{\text{pos}}(P, Q, R) = \frac{1}{2} (Q - P_y)^2 \quad (4)$$

with L_s as the length of the active contour

$$L_s = \int_0^{2\pi} R(t) dt. \quad (5)$$

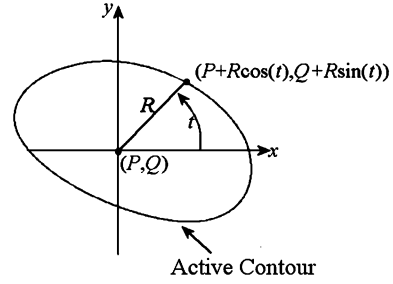


Fig. 4. Radial active contour.

Equation (1) represents a multicomponent energy functional, where E_{edge} is the additive inverse of the edge strength summed along the active contour and is normalized by the length of the contour. The function w appearing in (2) is an image edge potential surface. Thus, the minimum edge energy is attained when the active contour is residing on the ridges of the edge potential surface. The energy component E_{cons} is the constraint on the shape and size of a leukocyte. Assuming an approximately circular shape for the leukocyte, E_{cons} accounts for the deviations of its radial distances ($R(t)$) from the desired radius, ρ . In this formulation we assume y -axis to be perpendicular to the direction of the leukocyte rolling; the position constraint E_{pos} prevents large deviation of the active contour from the estimated direction of leukocyte rolling. In Section III-C we present a method to estimate the leukocyte motion direction.

The energy functional (1) contains three components with nonnegative weights μ_{cons} and μ_{pos} expressing the importance of the respective energy components in the functional. Parameter selection can be accomplished by the minimax [11] approach using a set of training sequences [20].

By way of variational calculus [8], the gradient descent equations for minimizing (1) are obtained as

$$\frac{\partial P}{\partial \tau} = \bar{w}_x \quad (6)$$

$$\frac{\partial Q}{\partial \tau} = \bar{w}_y - \mu_{\text{pos}}(Q - P_y) \quad (7)$$

$$\frac{\partial R(t)}{\partial \tau} = \frac{1}{L_s} \left(w + R(t) \frac{\partial w}{\partial x} \cos(t) + R(t) \frac{\partial w}{\partial y} \sin(t) - \bar{w} \right) - \mu_{\text{cons}}(R(t) - \rho) \quad (8)$$

where

$$\bar{w} = \frac{1}{L_s} \int_0^{2\pi} w(P + R(t) \cos(t), Q + R(t) \sin(t)) R(t) dt \quad (9)$$

$$\bar{w}_x = \frac{1}{L_s} \int_0^{2\pi} \frac{\partial w}{\partial x} (P + R(t) \cos(t), Q + R(t) \sin(t)) R(t) dt \quad (10)$$

and

$$\bar{w}_y = \frac{1}{L_s} \int_0^{2\pi} \frac{\partial w}{\partial y} (P + R(t) \cos(t), Q + R(t) \sin(t)) R(t) dt. \quad (11)$$

As described in steps 2a) and 2b) of **Algorithm 1**, starting from an initial contour $(P, Q, \text{ and } R)$, we employ the gradient descent (6)–(8) iteratively to obtain a new active contour configuration that minimizes (1) locally and delineates a leukocyte

in the process. The iterative gradient descent computation is referred to as active contour evolution [Step 2b)] of **Algorithm 1**.

Section II-B briefly reviews GVF and establishes the technical background for the proposed external force MGVF.

B. Gradient Vector Flow

The gradient descent (8) includes the terms $\partial w/\partial x$ and $\partial w/\partial y$, which are the x and the y -components of the edge force that attracts the active contour toward image edges. In our previous work [22], we have reported that instead of using the edge potential force, $\nabla|\nabla I|^2$, the use of GVF [31] in conjunction with the shape and size constrained active contour highly enhances the performance of tracking rolling leukocytes. To understand the supremacy of GVF over the edge potential force, let us imagine that the initial active contour is located away from the cell boundary and resides in a perfectly homogeneous region in an image. Using the traditional edge potential force leads to failure in such a case, because inside the homogeneous region, the image gradient magnitude would be zero and, consequently, there will be no edge-force acting on the active contour. Thus, being unable to sense the external force and being guided only by the internal force, the active contour may not move toward the desired edge. To alleviate this problem, Xu and Prince construct a force field by diffusing the edge-force, away from edges to the homogeneous regions, at the same time keeping the constructed field as close as possible to the edge-force near the edges. They achieve this goal through the minimization of the energy functional [31], as shown in (12) at the bottom of the page, where μ is a nonnegative parameter expressing the degree of smoothness of the field (u, v) , f is the edge potential: $f = |\nabla I|^2$, with I as the image under consideration. Interpretation of (12) is straightforward – the first term in the integrand keeps the field, (u, v) , smooth, while the second term forces the vectors to resemble the original edge-force near the edges (i.e., where the edge potential strength is high). Variational minimization of (12) results in the following two Euler equations [31]:

$$\begin{aligned}\mu \nabla^2 u - (f_x^2 + f_y^2)(u - f_x) &= 0 \\ \mu \nabla^2 v - (f_x^2 + f_y^2)(v - f_y) &= 0.\end{aligned}\quad (13)$$

Solving (13) for (u, v) results in a 2-D vector field – GVF that can be used as an external force field for the active contour.

III. MOTION GRADIENT VECTOR FLOW

A. Formulation

We have already demonstrated an example where the active contour fails to delineate a leukocyte with GVF as the external

force for the active contour. This situation frequently arises with **Algorithm 1**, when the frame-to-frame displacement of the leukocyte is large (i.e., greater than one cell radius). To seek a remedy, we propose to embed the leukocyte motion direction (can be estimated *a priori* utilizing microvessel shape information; see Section III-C) inside the energy for the GVF in the following way:

$$E_{\text{MGVF}}(w) = \frac{1}{2} \int \int [\mu H_\varepsilon(\nabla w \cdot (v^x, v^y)) |\nabla w|^2 + f(w - f)^2] dx dy. \quad (14)$$

where H_ε is a regularized heaviside function, f is the video frame edge-map: $f = |\nabla I|$, and (v^x, v^y) is the blood flow direction, known *a priori*. The first term in (14) smoothes the gradient of the image edge map, with a bias in the direction of flow, (v^x, v^y) . Here, the heaviside function $H_\varepsilon(\cdot)$ impedes diffusion of the vectors in the direction of blood flow. The second term forces the evolving gradient vectors at the actual boundaries to resemble the initial gradient vectors at the boundaries. μ is a nonnegative constant controlling the smoothness (diffusivity) imposed by the first term in the energy functional. We utilize the following regularized version of the heaviside function, parameterized by a small positive number ε :

$$H_\varepsilon(z) = \frac{1}{2} \left(1 + \frac{2}{\pi} \tan^{-1} \left(\frac{z}{\varepsilon} \right) \right). \quad (15)$$

Applying the variational principles for the minimization of (14) we obtain the following gradient descent equation (see the Appendix for derivation):

$$\frac{\partial w}{\partial \tau} = \mu \text{div}(H_\varepsilon(\nabla w \cdot (v^x, v^y)) \nabla w) - f(w - f). \quad (16)$$

Once w is obtained by solving (16), the gradient of w , viz., ∇w , serves the role of the external force for the active contour. The force field ∇w is referred to as the MGVF. Note from (16) that unlike GVF where the diffusion coefficient is constant, in MGVF the coefficient is dependent on ∇w , as well as the blood flow direction. Thus, the diffusion mechanism in MGVF is anisotropic.

B. Computation

To obtain a solution to (16), we follow an 8-neighborhood system on the discrete Cartesian image domain and utilize a Jacobian solution procedure as used in solving anisotropic diffusion equation [19], as shown in (17) at the bottom of the page, where $w_{i,j}^0 = f_{i,j}$, $w_{i,j}^\tau$, and $f_{i,j}$, respectively, denote the value of the surface w and the edge-map f at the (i, j) th location in the discrete domain, τ denotes the iteration number, and λ denotes inverse of the time-step. The following proposition illus-

$$E_{\text{GVF}}(u, v) = \frac{1}{2} \int \int \mu (u_x^2 + u_y^2 + v_x^2 + v_y^2) + (f_x^2 + f_y^2)((u - f_x)^2 + (v - f_y)^2) dx dy \quad (12)$$

$$w_{i,j}^{\tau+1} = w_{i,j}^\tau + \frac{\mu}{\lambda} \sum_{l=-1}^1 \sum_{m=-1}^1 H_\varepsilon((lv^y + mv^x)(w_{i+l,j+m}^\tau - w_{i,j}^\tau))(w_{i+l,j+m}^\tau - w_{i,j}^\tau) - \frac{1}{\lambda} f_{i,j}(w_{i,j}^\tau - f_{i,j}). \quad (17)$$

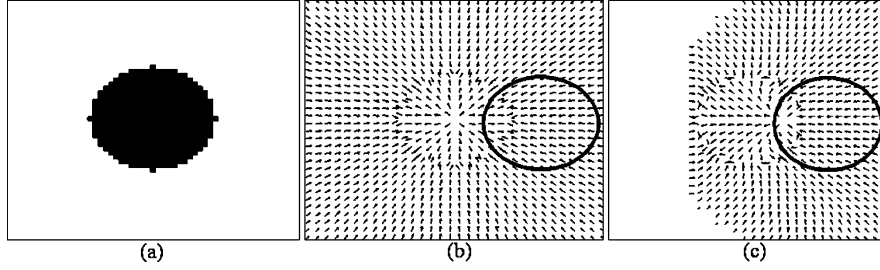


Fig. 5. (a) A circle representing a synthetic leukocyte, (b) GVF force for the circle and initial active contour, and (c) MGVF force for the circle and the same initial active contour.

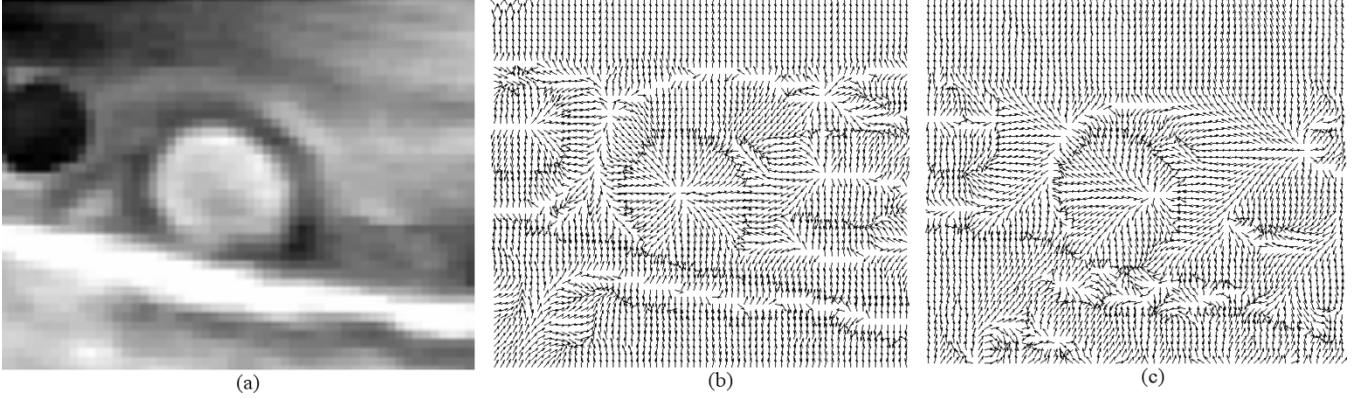


Fig. 6. (a) Leukocyte image of Fig. 3(a), (b) GVF and (c) MGVF for the leukocyte image.

trates the convergence conditions and the speed of convergence for (17).

Proposition 1: The numerical implementation given by (17) is convergent, and the rate of convergence is that of a geometric series of common ratio $(1 - \delta/\lambda)$, provided

- a) the edge-map f is normalized such that

$$0 < \delta \leq f_{i,j} \leq 1, \forall i, j \quad (18)$$

and

- b) we select the multiplicative inverse of the time-step as

$$\lambda \geq 1 + 8\mu. \quad (19)$$

Proof: See the Appendix .

Fig. 5(a) shows a synthetic leukocyte image, and Fig. 5(b) shows the GVF field of Fig. 5(a) and a lagging active contour. It is visually evident in Fig. 5(b) that the force is discouraging the active contour to delineate the proper leukocyte. Fig. 5(c) shows MGVF and the same lagging active contour. Due to the anisotropic diffusion of the vectors influenced by the motion direction, we can capture the leukocyte boundary despite the large displacement. The center from where the force arrows seem to emanate inside the circle in Fig. 5(b) is at the circle center, while the same point has been shifted toward right, near the circumference of the circle in Fig. 5(c). Note that in case of MGVF, the minimum value of w [of (17)] is attained at this point and thus the divergence of ∇w is the highest here creating the impression that force arrows emanate from this point. Fig. 6 illustrates GVF and MGVF for a real leukocyte image. In Section III-D by means of a simulation study with various values of the parameters μ and ε in the MGVF equation, we illustrate that the shift takes place consistently toward the edge and it stops at the edge.

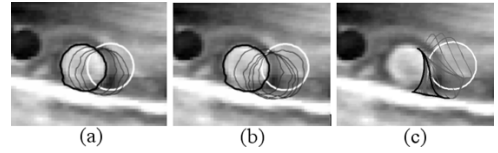


Fig. 7. MGVF active contour evolution. Frame-to-frame displacement is (a) small (on the order of one cell radius), and (b) large (approaching one cell diameter). In both these situations the contour evolution leads to object delineation. (c) Active contour evolution with MGVF but without a shape and size constraint. The contour fails to delineate the leukocyte.

Fig. 7(a) illustrates the leukocyte of Fig. 3(a) with an initial active contour identical to that of Fig. 3(b). Here the MGVF active contour captures the leukocyte, as does GVF. In Fig. 7(b), we use MGVF to delineate the leukocyte, where GVF fails as already indicated by Fig. 3(c). This is an example that demonstrates the efficacy of MGVF for both large and small frame-to-frame displacement of the leukocytes. However, we recognize that MGVF alone cannot recover leukocyte shapes, as shown in Fig. 7(c) for contour evolution with MGVF but without a shape-size constraint on the contour. In this case the contour fails to delineate the leukocyte boundary. We thus utilize both MGVF and shape-size constraint for the contour while tracking leukocytes.

Since *a priori* estimation of leukocyte movement direction is essential in MGVF computation the next section describes such a method.

C. Estimation of Leukocyte Rolling Direction

MGVF computation involves the *a priori* direction of leukocyte movement, which is essentially the direction of blood flow and can be approximated by the tangential direction to

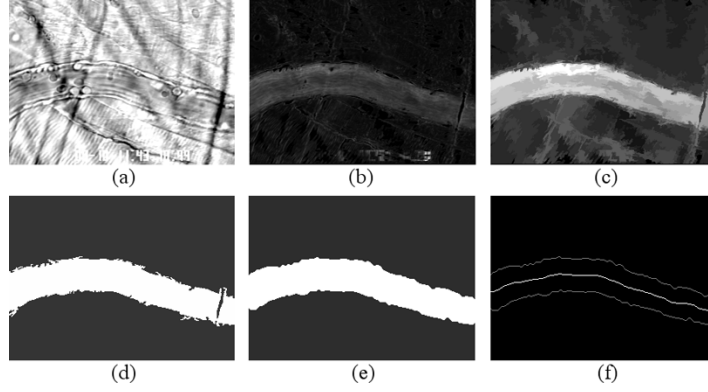


Fig. 8. (a) First frame of a sequence, (b) sum of absolute differences of consecutive frames for the sequence, (c) area open close of (b) with area scale of 500 pixels, (d) fuzzy *c*-means classification of (c), (e) morphological open-close of (d) with a circular structuring element of radius 3, (f) boundaries of the microvessel and the microvessel centerline, *i.e.*, the path of leukocyte rolling.

the centerline of the microvessel. Thus, we detect two microvessel boundaries from a video sequence; then compute the centerline that is midway between these two boundaries. The first step toward the centerline computation is to register the video frames. We employ a template matching method for video frame registration. The template in this case is the entire intensity profile of the first frame of a sequence. The match measure is normalized cross correlation, where jitter is assumed to be caused by a single global translation. Previous studies support the assumption of global translation for the intravital microscopic experiments [13], [25]. Thus, every frame in the sequence is registered with respect to the first frame of the sequence. Tang and Acton [28] find the microvessel boundaries by active contour-based method; however, we employ fuzzy *c*-means classification [5] that produces reasonably accurate results and is computationally inexpensive. The method is described in the following sequential steps:

- 1) *Computation of average of absolute differences (D):* Let I_1, I_2, \dots, I_n be the registered video frames of a sequences, then D is computed as: $D(i, j) = 1/(n-1) \sum_{k=2}^n |I_k(i, j) - I_{k-1}(i, j)|$. **Fig. 8(a)** shows the first image of a video sequence. **Fig. 8(b)** shows the average of absolute difference image, D , for this video sequence.
- 2) *Computation of area open-closed image:* Area open (close) refers to a connected filter that retains foreground (background) connected components of every possible level set of a gray scale image, the area for which is greater than or equal to a certain value [2]. Here, the term *level set* refers to a binary image obtained by thresholding the original gray level image at a gray level. The area value with which area opening or area closing is performed referred to as a “scale.” Thus, if I is the original gray scale image, O_s and C_s are, respectively, the area open and area close operators at a scale s , then the area-open close of I at scale s is $I_s = C_s(O(I))$. Typically a leukocyte has a diameter of $8 \mu\text{m}$. So it has an area of about $50 \mu\text{m}^2$ (which equates to roughly 290 pixels with the spatial resolution of our experiments). The microvessel on the other hand is typically $100 \mu\text{m} \times 20 \mu\text{m}$ (about 11 560 pixels in our system). Thus, we need to choose an area scale over 290 pixels but below 11 560

pixels. We observe that an area scale of 500 pixels suffices. **Fig. 8(c)** shows $D_{500} = C_{500}(O_{500}(D))$.

- 3) *Classification of area open-closed image:*

We consider fuzzy *c*-means classification [5] of the area open-closed image, $D_{500} = C_{500}(O_{500}(D))$, based on its gray values. **Fig. 8(d)** shows fuzzy *c*-means classification of D_{500} into two classes (inside and outside of the microvessel).

- 4) *Postprocessing:* Since fuzzy *c*-means classification in most of the cases provide a rough boundary of the microvessel and sometimes partly broken in the middle (as shown in **Fig. 8(d)**), we make the boundary smooth by morphological close-open filter [27]. We obtain **Fig. 8(e)** after smoothing **Fig. 8(d)** with a morphological close-open filter.

- 5) *Computation of microvessel centerline:* The final step is to find out the edge of the microvessel and obtain the mean leukocyte rolling path that is midway between the microvessel boundaries. In order to compute this mean path, we first compute the skeleton (via medial axis transformation) [27] of the binary image shown in **Fig. 8(e)**, next we take longest path [27] in the skeleton as the microvessel centerline, which is shown in **Fig. 8(f)**.

Note that the method described thus far is a special case of the scale-space segmentation technique proposed by Acton and Mukherjee in [2], where area open-close is performed on the same image in general for $N (> 1)$ area scales to generate N filtered images collectively called a scale-space. Then pixel locations are classified based on the entire scale-space, *i.e.*, each spatial pixel is classified using a vector of N values from the N scale-space images. Here instead we employ the classification technique on a single area scale since we need only two classes.

Although leukocyte velocity direction is crucial information to MGVF computation and subsequent tracking, the following example illustrates that correct tracking results may be obtained even when leukocyte movement direction varies significantly from the assumed/estimated direction. In Fig. 9(a) we illustrate a microvessel boundary obtained via segmentation, the centerline of the microvessel and the manually computed leukocyte path. The figure indicates that actual leukocyte movement direction in this case is quite different from the direction of the centerline velocity for the vessel. However, the active contour tracking of

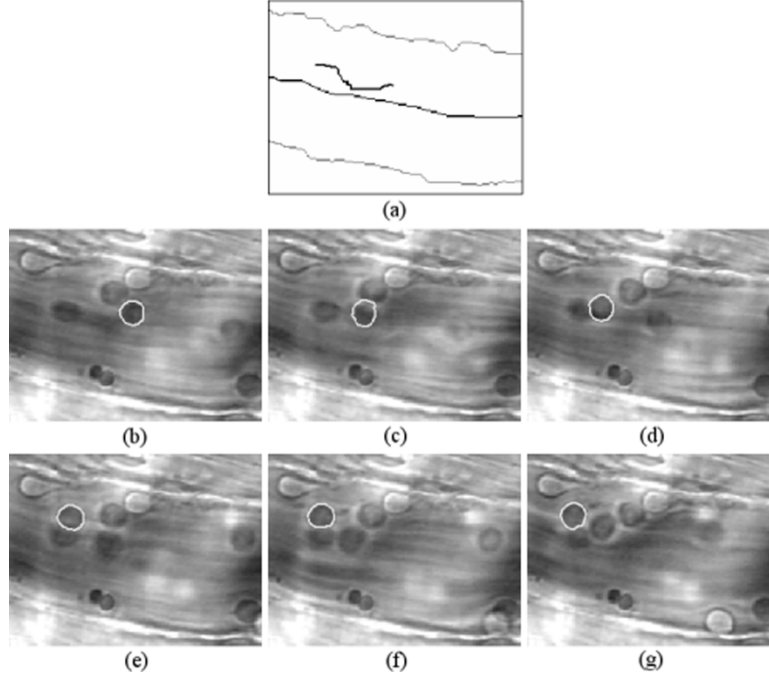


Fig. 9. (a) Microvessel boundary outlines, microvessel centerline and manually computed leukocyte path for a sequence – (b) 1st frame, (c) 11th frame, (d) 21st frame, (e) 31st frame, (f) 41st frame, (g) 51st frame. Tracking by MGVF guided shape and size constrained active contour is shown on all the frames.

the leukocyte via MGVF and shape-size constraints proceeds without any error as shown in Fig. 9(b)–(g). This leukocyte sequence can be considered as a relatively 'fast' sequence, since the interframe leukocyte displacement exceeded one leukocyte radius in a number of frames. We have observed that the simultaneous occurrence of a) high interframe leukocyte displacement and b) leukocyte movement direction that is significantly different from the estimated motion direction can lead to failure of the MGVF-driven active contour.

The next section illustrates one-dimensional (1-D) simulation for MGVF that indicates the roles of the parameters involved in the MGVF functional.

D. One-Dimensional Simulation

For the convenience of representation, we carry out the simulation in one dimension. The 1-D MGVF equation is as follows:

$$w_j^{\tau+1} = w_j^{\tau} + \frac{\mu}{1+2\mu} \sum_{m=-1}^1 H_{\varepsilon}((mv)(w_{j+m}^{\tau} - w_j^{\tau}))(w_{j+m}^{\tau} - w_j^{\tau}) - \frac{1}{1+2\mu} f_j(w_j^{\tau} - f_j) \quad (20)$$

$$w_j^0 = f_j$$

where v is the direction of flow; $v = 1$ and $v = -1$, respectively, denote movement to right or left. The topmost image of Fig. 10 shows a 1-D signal, the second image from top shows the edge response for the signal. 1-D MGVF computation with $v = -1$ and f as the edge response in (20) yields w as shown in the third image (from the top) in Fig. 10. The minimum value of w within the step edge indicators is marked with asterisk on the same image. The sign of dw/dx is shown in the fourth image of Fig. 10. The sign image indicates that the sign of dw/dx is different on the two sides of the asterisk (location of lowest

value of w). The second image from bottom in Fig. 10 shows w computed via (20) with $v = 0$. And the corresponding sign image is shown in the bottom image of Fig. 10. $v = 0$ imposes the lowest value of w at the midpoint of the edge responses.

With this preliminary MGVF computation we observe that $v = -1$ shifts the lowest point of w to the right, and the slope of w is negative (positive) to the left (right) of the lowest point. Any point to the left (right) of the lowest point of w is attracted to the left (right) edge because of the slope of w . Similarly, in two dimensions, once an active contour, possibly lagging far behind the leukocyte, includes this lowest point within its periphery, the contour is attracted to the leukocyte boundary. Therefore, for successful leukocyte boundary delineation, the lowest point of w must be inside the initial active contour. We carry out a 1-D simulation illustrated in Fig. 11 to show that the lowest point of w will be located at the right edge regardless of the value of μ , when ε is sufficiently small. Fig. 11 shows computed w values via (20) corresponding to various values of μ and ε with $v = -1$ on a noise-free 1-D signal. We observe from the simulation that for any value of μ (between 0.01 and 10), there is always a value of ε below which the lowest point of w will be located at the right edge position. Note that the shift is monotonic with decreasing ε , and once the right edge location is reached, the lowest point of w does not shift any more even if ε is decreased further. From this simulation we observe that: 1) the shift of the minimum point of w occurs in the opposite direction of the velocity, and this minimum does not move beyond edges; 2) the choice of μ is insignificant for noise-free ideal images, since with a sufficiently small ε , the lowest point of w is located at the edge; 3) larger values of μ require lower values of ε for moving the lowest point of w to the edge. The second two observations suggest that if we choose a small value for ε , then, even if the lagging active contour from previous frame barely overlaps with

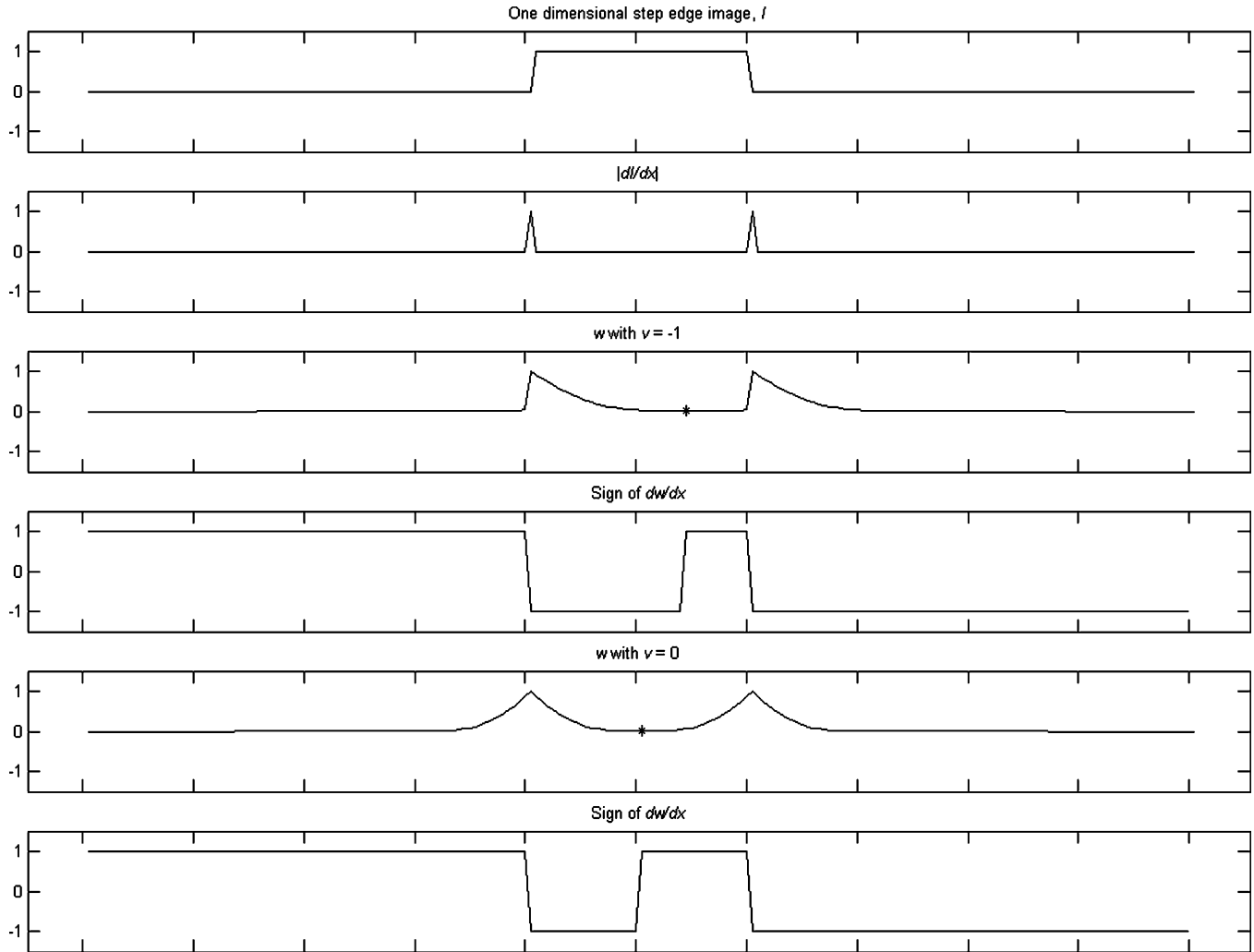


Fig. 10. Step edge and MGVF in one dimension.

the present leukocyte position, MGVF is expected to align the active contour onto the leukocyte boundary.

IV. TRACKING EXPERIMENTS

We consider two test data sets for the tracking experiments. The first test data set consists of 100 intravital microscopic video sequences each 91 frames long (3 s in duration). These sequences are captured from experiments involving wild type and knockout mice [18]. The video frames have been recorded at a spatial resolution of 320×240 pixels, where the pixel-to-micron ratio is 2.47 pixels/micron horizontally and 2.34 pixels/micron vertically, and the temporal resolution is 30 frames/s. The second data set consists of 25 intravital microscopic video sequences each 31 frames long (1-s duration) obtained from experiments with trauma-induced untreated mice [22]. The second data set has been captured at a higher spatial resolution (3.11 pixels/micron horizontally and 3.10 pixels/micron vertically) and with the same temporal resolution of 30 frames/s. The frame-to-frame displacements of the leukocytes in the second data set are higher than those in the first data set. To compare the tracking performance of MGVF to that of GVF, we utilize manually determined leukocyte center locations.

For an error measure, we employ the root mean-squared error (RMSE), measured in microns, between the tracker-computed and the manually determined leukocyte center within each frame. Through the use of minimax method, we found that $\mu_{\text{cons}} = 0.1$ and $\mu_{\text{pos}} = 0.2$ are suitable for the tracking within these data sets [20]. And, from the simulation study we learn that a small value of ε for MGVF is advisable. We choose ε as 10^{-5} for all the tracking experiments reported here.

To compare tracking results using GVF and MGVF as the external force for the active contour, it is necessary to study the sensitivity to the parameter μ . For this purpose, we randomly choose 15 leukocyte sequences from the data set consisting of 100 sequences and run tracking experiments on them for different values of μ for computing GVF and MGVF. The average error values obtained after such experiments are reported through Fig. 12(a) and (b). We have displayed results for two different ranges of weighting parameter values – Fig. 12(a) showing [0.01, 0.1] and Fig. 12(b) showing [0.1, 1.0]. We observe in both these cases that MGVF outperforms GVF tracking results for all corresponding values of weighting parameters. Also note that the overall minimum error for MGVF is less than that of GVF within the range [0.01, 1.0]. In the subsequently reported tracking experiments, we choose μ as 0.08.

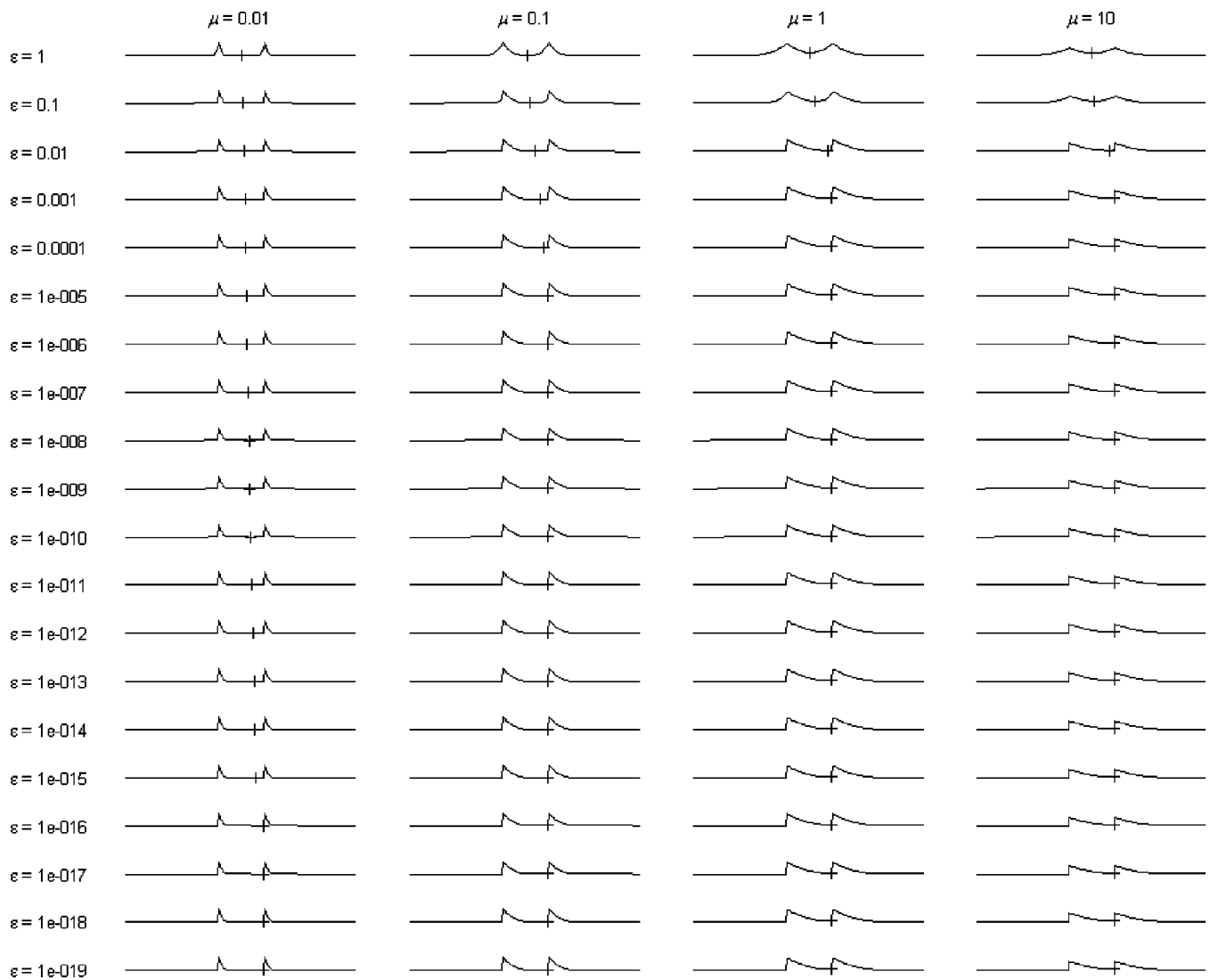


Fig. 11. One-dimensional MGVF simulation study showing w computed with (20) for various values of μ and ε .

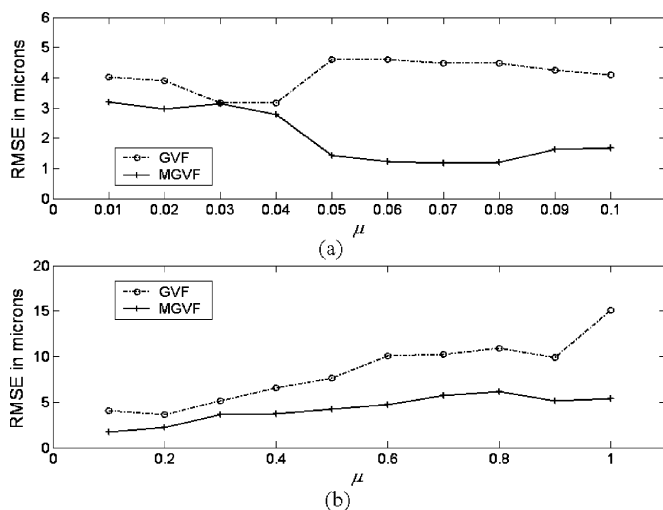


Fig. 12. Comparison of GVF and MGVF tracking performance for different values of weighting parameters.

In the first tracking experiment on the 25-sequence data set, we utilize three “rules” of contour advancement for GVF: an initial position shifted in blood flow direction by 1) half the leuko-

TABLE I
AVERAGE RMSES (IN μm) FOR FOUR METHODS OF TRACKING

MGVF	GVF with no shift	GVF with $R/2$ shift	GVF with R shift
1.9	4.3	2.8	10.3

cyte radius, 2) one leukocyte radius, and 3) no shift at all. Next we perform MGVF tracking on these 25 sequences, utilizing the computed leukocyte rolling direction. In Fig. 13, we show RMSEs for the leukocyte sequences arranged in the increasing order of the manually observed average rolling velocity. For the four tracking experiments Table I shows RMSEs averaged over all the 25 sequences.

As mentioned in Section I, the leukocytes show complex traits of motion—sometimes they adhere to the endothelial wall and often they show microbursts or leaps in position. Thus, advancing the contour in the direction in the motion has the risk that the contours may be attracted to clutter; this is reflected in the results (Fig. 13 and Table I) where contours are advanced by one full leukocyte radius. On the other hand, not advancing the contour at all has the risk that the contours get attracted to the

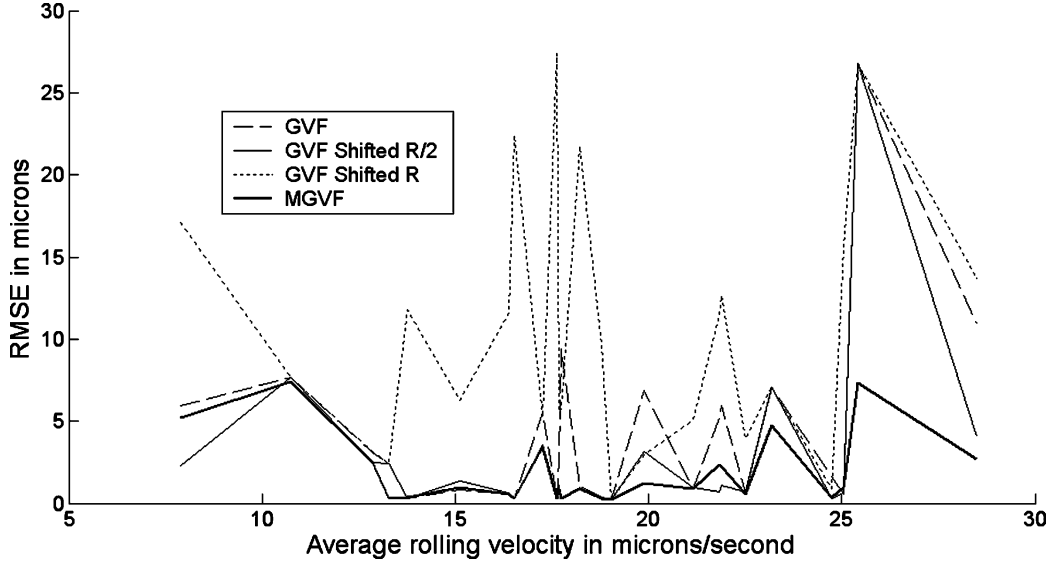


Fig. 13. Tracking performance vs. average rolling velocity. GVF: no advancement of initial active contour. GVF Shifted $R/2$: initial active contour advanced by half the leukocyte radius, R . GVF Shifted R : initial active contour advanced by half the leukocyte radius.

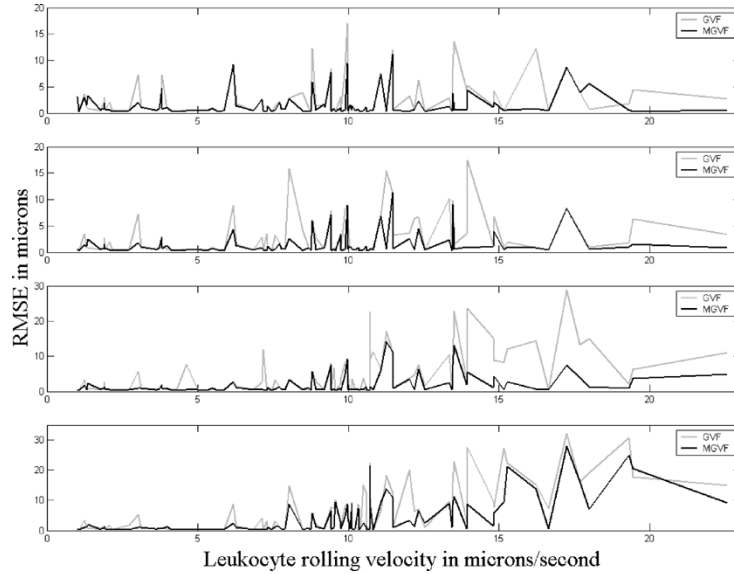


Fig. 14. From top to bottom order – GVF versus MGVF tracking performance with original, half, one-third and one-fourth frame rate. x -axis represents leukocyte rolling velocity (manually found) in microns/s and y -axis represents tracking error in microns.

clutter when the leukocyte moves ahead. When the advancement of the contour is half the leukocyte radius, the RMSE error is less than aforementioned two cases (Table I). Because, in this case the tracker tries to achieve a balance between the two situations: 1) where the leukocytes are adherent; 2) where the cells make bursts in motion as large as one full leukocyte radius. However, MGVF tracker outperforms these three GVF trackers as noted in Table I. The performance MGVF tracker is comparable to those of GVF in the lower velocity range ($< 16 \mu\text{m/s}$). However, note from Fig. 13 that as the leukocyte velocity increases, the MGVF performance significantly exceeds that of the GVF trackers. The experiment validates our motivation behind MGVF – when frame-to-frame displacement of leukocytes is large, MGVF will be effective.

Our second tracking experiment involves the 100-sequence data set. Using this data set, we perform GVF and MGVF

tracking on successively decreasing temporal resolutions (i.e., increasing frame-to-frame displacements). Four temporal resolutions are considered: 1) original resolution, i.e., every frame in the sequence is considered; 2) half resolution, i.e., every other frame is considered; 3) one-third resolution; 4) one-fourth resolution. For all four temporal resolutions, we perform GVF as well as MGVF tracking. The results are shown in Fig. 14. Table II, shows the summary of these results by providing only the average RMSEs computed over the 100 sequences for all the four temporal resolutions. The results show that the performance of GVF deteriorates as the frame rate decreases, whereas the performance of MGVF remains almost the same for first three frame rates and decreases (at a rate less than that of GVF) for the one-fourth frame rate. Again this experiment demonstrates that when the frame-to-frame displacement of leukocytes increases, the MGVF tracker outperforms GVF

TABLE II
AVERAGE RMSE (IN μm) OF GVF AND MGVF TRACKING METHODS FOR FOUR FRAME RATES

	Original frame rate (30 fps)	Half frame rate (15 fps)	One-third frame rate (10 fps)	One-fourth frame rate (7.5 fps)
Mean RMSE for GVF tracking	2.5	2.7	4.3	6.0
Mean RMSE for MGVF tracking	1.6	1.5	1.8	3.9

tracker, because in the latter case the contour lags far behind the leukocyte and there is no mechanism to drag the contour toward the leukocyte. Note also that the MGVF tracking RMSE increases when the frame rate is one-fourth the original rate and the average velocity is large ($> 16 \mu\text{m/s}$), because in such cases, frame-to-frame displacements are so high sometimes that the lagging contours barely overlap or do not overlap at all with the leukocytes.

V. CONCLUSION

In this paper, we introduce a novel external force for tracking rolling leukocytes observed in intravital video microscopy. Unlike existing active contour force models, such as GVF, MGVF utilizes the direction of leukocyte movement. We show that while GVF is unsuitable for tracking fast rolling leukocytes, MGVF is well adapted to both fast and slow rolling. Equivalently, MGVF performs well when the temporal resolution of a leukocyte rolling sequence is reduced, and thus can be used to increase throughput. We also show that MGVF computation is numerically convergent and the rate of convergence is that of an equivalent geometric series.

APPENDIX

MINIMIZATION OF MGVF ENERGY FUNCTIONAL

Minimization of MGVF energy functional can be achieved with variational calculus [8], [30] as follows. The first variation of (14) with respect to w is obtained by adding a small perturbation function $\alpha q(x, y)$ to $w(x, y)$, and taking the derivative with respect to α , as shown in (21) at the bottom of the page. Now, applying the Mean Value Theorem [24]

$$H_\varepsilon(\nabla w \cdot (v^x, v^y) + \alpha \nabla q \cdot (v^x, v^y)) - H_\varepsilon(\nabla w \cdot (v^x, v^y)) = \alpha \nabla q \cdot (v^x, v^y) H'_\varepsilon(\nabla w \cdot (v^x, v^y) + \alpha \theta \nabla q \cdot (v^x, v^y)) \quad (22)$$

where $\theta(x, y)$ is a function with $0 < \theta(x, y) < 1, \forall x, y$. Using (22) in (21), we obtain

$$\begin{aligned} \lim_{\alpha \rightarrow 0} \frac{E_{\text{MGVF}}(w + \alpha q) - E(w)}{\alpha} &= \frac{1}{2} \int \int \mu(|\nabla w|^2 H'_\varepsilon(\nabla w \cdot (v^x, v^y)) \nabla q \cdot (v^x, v^y)) dx dy \\ &\quad + \int \int (\mu H_\varepsilon(\nabla w \cdot (v^x, v^y)) \nabla w \cdot \nabla q) dx dy \\ &\quad + \int \int (f(w - f)q) dx dy \end{aligned} \quad (23)$$

where

$$H'_\varepsilon(z) = \frac{dH(z)}{dz} = \frac{1}{\pi} \left(\frac{\varepsilon}{z^2 + \varepsilon^2} \right). \quad (24)$$

Now for the first integral in (23) the following can be deduced using (24):

$$\begin{aligned} &\left| \int \int \mu(|\nabla w|^2 H'_\varepsilon(\nabla w \cdot (v^x, v^y)) \nabla q \cdot (v^x, v^y)) dx dy \right| \\ &= \left| \frac{\mu}{\pi} \int \int \frac{\varepsilon |\nabla w|^2 \nabla q \cdot (v^x, v^y)}{|\nabla w \cdot (v^x, v^y)|^2 + \varepsilon^2} dx dy \right| \\ &\leq \frac{\varepsilon \mu}{\pi} \int \int \frac{|\nabla w|^2 |\nabla q \cdot (v^x, v^y)|}{|\nabla w \cdot (v^x, v^y)|^2} dx dy. \end{aligned} \quad (25)$$

From (25) we readily observe that except when gradient of w is perpendicular or nearly perpendicular to the leukocyte flow velocity (v^x, v^y) , the contribution of the first integral in (23) is negligible for small values of ε . On the other hand, the minimization of MGVF energy functional (14) should lead to small $|\nabla w|$, when ∇w is perpendicular or nearly perpendicular to the flow velocity. In other words we may assume that when $|\nabla w \cdot (v^x, v^y)|$ is infinitesimal so is $|\nabla w|$, i.e.,

$$\begin{aligned} \lim_{\alpha \rightarrow 0} \frac{E_{\text{MGVF}}(w + \alpha q) - E(w)}{\alpha} &= \lim_{\alpha \rightarrow 0} \left[\frac{1}{2\alpha} \int \int \mu |\nabla w|^2 (H_\varepsilon(\nabla w \cdot (v^x, v^y) + \alpha \nabla q \cdot (v^x, v^y)) - H_\varepsilon(\nabla w \cdot (v^x, v^y))) dx dy \right. \\ &\quad + \alpha \int \int (\mu H_\varepsilon(\nabla w \cdot (v^x, v^y) + \alpha \nabla q \cdot (v^x, v^y)) \nabla w \cdot \nabla q) dx dy \\ &\quad + \frac{\alpha^2}{2} \int \int (\mu H_\varepsilon(\nabla w \cdot (v^x, v^y) + \alpha \nabla q \cdot (v^x, v^y)) |\nabla q|^2) dx dy \\ &\quad \left. + \alpha \int \int (f(w - f)q) dx dy + \frac{\alpha^2}{2} \int \int (f q^2) dx dy \right] \end{aligned} \quad (21)$$

$|\nabla w|/(|\nabla w \cdot (v^x, v^y)|) \approx 1$ for small $|\nabla w \cdot (v^x, v^y)|$. Thus, in such cases we have

$$\frac{\varepsilon\mu}{\pi} \iint \frac{|\nabla w|^2 |\nabla q \cdot (v^x, v^y)|}{|\nabla w \cdot (v^x, v^y)|^2} dx dy \approx \frac{\varepsilon\mu}{\pi} \iint |\nabla q \cdot (v^x, v^y)| dx dy. \quad (26)$$

From (26) we observe that for small values of ε the first integral in (23) is negligible when ∇w is perpendicular or nearly perpendicular to the flow velocity. Therefore, we neglect the contribution of the first integral of (23) whether or not ∇w is perpendicular to the flow velocity and now we are only left with the second and the third integral of (23).

Applying Green's theorem [24] to the second integral of (23) we obtain

$$\begin{aligned} & \iint (\mu H_\varepsilon(\nabla w \cdot (v^x, v^y)) \nabla w \cdot \nabla q) dx dy \\ &= \int_{\partial\Omega} \mu q H_\varepsilon(\nabla w \cdot (v^x, v^y)) \nabla w \cdot d\sigma \\ & - \iint (\mu q \operatorname{div}(H_\varepsilon(\nabla w \cdot (v^x, v^y)) \nabla w)) dx dy. \end{aligned} \quad (27)$$

Thus, disregarding the first integral of (23), combining (23) with (27) and applying the boundary condition: $\nabla w \cdot \mathbf{n}_{\partial\Omega} = 0$ on $\partial\Omega$, where $\mathbf{n}_{\partial\Omega}$ denotes the perpendicular to the boundary $\partial\Omega$, we obtain

$$\lim_{\alpha \rightarrow 0} \frac{E_{\text{MGVF}}(w + \alpha q) - E(w)}{\alpha} = \iint ((f(w - f) - \mu \operatorname{div}(H_\varepsilon(\nabla w \cdot (v^x, v^y)) \nabla w)) q) dx dy. \quad (28)$$

So the first variation of the energy functional (14) obtained from (28) is as follows [30]:

$$\frac{\delta E_{\text{MGVF}}}{\delta w} = -\mu \operatorname{div}(H_\varepsilon(\nabla w \cdot (v^x, v^y)) \nabla w) + f(w - f). \quad (29)$$

And now the gradient descent equation to obtain the minimizing function w is as follows:

$$\frac{\partial w}{\partial \tau} = -\frac{\delta E_{\text{MGVF}}}{\delta w} = \mu \operatorname{div}(H_\varepsilon(\nabla w \cdot (v^x, v^y)) \nabla w) - f(w - f).$$

Proof of Proposition 1

If r denotes the location (i, j) , then (17) can be rewritten as

$$w_r^{\tau+1} = \left(1 - \frac{f_r}{\lambda} - \frac{\mu}{\lambda} \sum_{q \in N(r)} c_q^\tau\right) w_r^\tau + \frac{\mu}{\lambda} \sum_{q \in N(r)} c_q^\tau w_q^\tau + \frac{f_r^2}{\lambda} \quad (30)$$

where $N(r)$ denotes the 8 neighbors of the location r and c_q^τ is as follows:

$$c_q^\tau = H_\varepsilon((lv^x + mv^y)(w_q^\tau - w_r^\tau)) \quad (31)$$

where (l, m) denotes the vector representing the direction from location r to the location q in $N(r)$, and (v^x, v^y) denotes the leukocyte velocity direction. Let us now impose the following:

$$\lambda \geq \max_r \left(f_r + \mu \sum_{q \in N(r)} c_q^\tau \right) \quad (32)$$

then all the coefficients of w 's in (30) become nonnegative. Equation (30) can be rewritten for all the grid locations of the image domain in a matrix-vector form as follows:

$$\mathbf{w}^{\tau+1} = A^\tau \mathbf{w}^\tau + \mathbf{f} \quad (33)$$

where A^τ is a $M \times M$ matrix, M being the total number of grid points in the image domain. A^τ has all nonnegative elements and any of its row contains at the most 9 positive elements. \mathbf{f} and \mathbf{w}^τ are column vectors given as follows:

$$\mathbf{f} = \left[\frac{f_1^2}{\lambda} \dots \frac{f_M^2}{\lambda} \right]^T, \quad \mathbf{w}^\tau = [w_1^\tau \dots w_M^\tau]^T. \quad (34)$$

We can rewrite (33) as follows:

$$\begin{aligned} \mathbf{w}^{\tau+1} &= A^\tau A^{\tau-1} \dots A^0 \mathbf{w}^0 + (A^\tau A^{\tau-1} \dots A^1) \mathbf{f} \\ &+ (A^\tau A^{\tau-1} \dots A^2) \mathbf{f} + \dots + (A^\tau) \mathbf{f} + \mathbf{f}. \end{aligned} \quad (35)$$

If we now impose condition (18) on the edge-map, then it can be shown that

$$\begin{aligned} (\mathbf{f})_r &\leq \frac{1}{\lambda}, (A^\tau \mathbf{f})_r \\ &\leq \left(1 - \frac{\delta}{\lambda}\right) \frac{1}{\lambda}, \dots, ((A^\tau A^{\tau-1} \dots A^{\tau-i+1}) \mathbf{f})_r \\ &\leq \left(1 - \frac{\delta}{\lambda}\right)^i \frac{1}{\lambda}, \quad \forall r \end{aligned}$$

where $(\mathbf{x})_r$ denotes the r th element of the vector \mathbf{x} . Now, note that (35) is a series with nonnegative terms, so by the comparison test with a geometric series of common ratio: $0 < (1 - \delta/\lambda) < 1$, (35) converges as $\tau \rightarrow \infty$. Finally from (31) we note that the maximum value a coefficient, c_q^τ , can achieve is unity; also the maximum value of the normalized edge-map f_r is unity. Therefore, the right hand side of (32) never exceeds $1 + 8\mu$ assuming an 8-neighborhood, consequently we make λ as $1 + 8\mu$ in the numerical implementation of (17).

REFERENCES

- [1] S. T. Acton and K. Ley, "Tracking leukocytes from *in vivo* video microscopy using morphological anisotropic diffusion," in *Proc. IEEE Int. Conf. Image Proc. 2001*, vol. 2, pp. 300–303.
- [2] S. T. Acton and D. P. Mukherjee, "Scale space classification using area morphology," *IEEE Trans. Image Processing*, vol. 9, pp. 623–635, Apr. 2000.
- [3] S. T. Acton, K. Wethmar, and K. Ley, "Automatic tracking of rolling leukocytes *in vivo*," *Microvasc. Res.*, vol. 63, pp. 139–148, 2002.
- [4] C. M. Anderson, G. N. Georgiou, I. E. G. Morrison, G. V. W. Stevenson, and R. J. Cherry, "Tracking of cell surface receptors by fluorescence digital imaging microscopy using a charge-coupled device camera," *J. Cell Sci.*, vol. 101, pp. 415–425, 1992.

- [5] J. C. Bezdek, *Pattern Recognition with Fuzzy Objective Function Algorithms*. New York: Plenum, 1981.
- [6] A. Chakraborty, L. H. Staib, and J. S. Duncan, "Deformable boundary finding in medical images by integrating gradient and region information," *IEEE Trans. Med. Imag.*, vol. 15, pp. 859–870, Dec. 1996.
- [7] T. F. Chan and L. A. Vese, "Active contour without edges," *IEEE Trans. Image Processing*, vol. 10, pp. 266–277, Feb. 2001.
- [8] R. Courant and D. Hilbert, *Methods of Mathematics Physics*. New York: Interscience, 1953, vol. 1.
- [9] J. A. DiVietro, M. J. Smith, B. R. Smith, L. Petruzzelli, R. S. Larson, and M. B. Lawrence, "Immobilized IL-8 triggers progressive activation of neutrophils rolling *in vitro* on P-selectin and intercellular adhesion molecule-1," *J. Immunol.*, vol. 167, pp. 4017–4025, 2001.
- [10] J. Gelles, B. J. Schnapp, and M. P. Sheetz, "Tracking kinesin-driven movements with nanometer-scale precision," *Nature*, vol. 331, pp. 450–453, 1988.
- [11] M. A. Gennert and A. Y. Yuille, "Determining the optimal weights in multiple objective function optimization," in *Proc. 2nd Int. Conf. Computer Vision*, 1988, pp. 87–89.
- [12] R. N. Ghosh and W. W. Webb, "Automated detection and tracking of individual and clustered cell surface low density lipoprotein receptor molecules," *Biophys. J.*, vol. 66, pp. 1301–1318, 1994.
- [13] A. P. Goobic and S. T. Acton, "Image stabilization and registration for tracking cells in the microvasculature," *IEEE Trans. Biomed. Eng.*, 2005, to be published.
- [14] A. P. Goobic, M. E. Welsner, S. T. Acton, and K. Ley, "Biomedical application of target tracking in clutter," in *Proc. 35th Asilomar Conf. Signals, Systems and Computers*, vol. 1, 2001, pp. 88–92.
- [15] W. H. Guilford and R. W. Gore, "The mechanics of arteiole-interstitium interaction," *Microvasc. Res.*, vol. 50, pp. 260–287, 1995.
- [16] A. Hafezi-Moghadam, K. L. Thomas, A. J. Prorock, Y. Huo, and K. Ley, "L-selectin shedding regulates leukocyte recruitment," *J. Exp. Med.*, vol. 193, no. 7, pp. 863–872, 2001.
- [17] A. Kusumi, Y. Sako, and M. Yamamoto, "Confined lateral diffusion of membrane receptors as studied by single particle tracking (Nanovid microscopy). Effects of calcium-induced differentiation in cultured endothelial cells," *Biophys. J.*, vol. 65, pp. 2021–2040, 1993.
- [18] K. Ley, "Leukocyte recruitment as seen by intravital microscopy," in *Physiology of Inflammation*, K. Ley, Ed. New York: Oxford Univ. Press, 2001, pp. 303–337.
- [19] P. Perona and J. Malik, "Scale-space and edge detection using anisotropic diffusion," *IEEE Trans. Pattern Anal. Machine Intell.*, vol. 12, pp. 629–639, July 1990.
- [20] N. Ray, "Tracking rolling leukocytes *in vivo* using active contours with motion gradient vector flow," Ph.D. dissertation, Univ. Virginia, Charlottesville, 2003.
- [21] N. Ray and S. T. Acton, "Detection and tracking of rolling leukocytes from intravital microscopy," in *Proc. IEEE Int. Symp. Biomedical Imaging (ISBI04)*, Arlington, VA, April 2004, pp. 15–18.
- [22] N. Ray, S. T. Acton, and K. Ley, "Tracking leukocytes *in vivo* with shape and size constrained active contours," *IEEE Trans. Med. Imag. (Special issue on Image Analysis in Drug Discovery and Clinical Trials)*, vol. 21, pp. 1222–1235, Oct. 2002.
- [23] N. Ray, S. T. Acton, T. Altes, E. E. de Lange, and J. R. Brookeman, "Merging parametric active contours within homogeneous image regions for MRI-based lung segmentation," *IEEE Trans. Med. Imag.*, vol. 22, pp. 189–199, Feb. 2003.
- [24] W. Rudin, *Principles of Mathematical Analysis*, 3rd ed. New York: McGraw-Hill, 1976.
- [25] Y. Sato, J. Chen, R. A. Zoroofi, N. Harada, S. Tamura, and T. Shiga, "Automatic extraction and measurement of leukocyte motion in microvessels using spatiotemporal image analysis," *IEEE Trans. Biomed. Eng.*, vol. 44, pp. 225–236, Apr. 1997.
- [26] G. J. Schütz, H. Schindler, and T. Schmidt, "Single-molecule microscopy on model membranes reveals anomalous diffusion," *Biophys. J.*, vol. 73, pp. 1073–1080, 1997.
- [27] P. Soille, *Morphological Image Analysis*. Berlin, Germany: Springer-Verlag, 1999.
- [28] J. Tang and S. T. Acton, "Vessel boundary tracking for intravital microscopy via multilevel gradient vector flow snakes," *IEEE Trans. Biomed. Eng.*, vol. 51, pp. 316–324, Feb. 2004.
- [29] A. Tsai, A. Yezzi, and A. S. Willsky, "Curve evolution implementation of the Mumford-Shah functional for image segmentation, denoising, interpolation, and magnification," *IEEE Trans. Image Processing*, vol. 10, pp. 1169–1186, Aug. 2001.
- [30] J. L. Troutman, *Variational Calculus with Elementary Convexity*. New York: Springer-Verlag, 1983.
- [31] C. Xu and J. L. Prince, "Snakes, shapes, and gradient vector flow," *IEEE Trans. Image Processing*, vol. 7, pp. 359–369, Mar. 1998.
- [32] C. Zimmer, E. Labruyere, V. Meas-Yedid, N. Guillen, and J. C. Olivo-Marin, "Segmentation and tracking migrating cells in videomicroscopy with parametric active contours: A tool for cell-based drug testing," *IEEE Trans. Med. Imag. (Special issue on Image Analysis in Drug Discovery and Clinical Trials)*, vol. 21, pp. 1212–1221, Oct. 2002.